# Use of flexible micro-temperature sensor to determine temperature *in situ* and to simulate a proton exchange membrane fuel cell

Chi-Yuan Lee [a,*], Fang-Bor Weng [a], Chin-Hsien Cheng [a], Huan-Ruei Shiu [b], Shiqah-Ping Jung [b], Wen-Chen Chang [b], Pin-Cheng Chan [a], Wen-Ting Chen [a], Chung-Ju Lee [a]

[a] Department of Mechanical Engineering, Yuan Ze Fuel Cell Center, Yuan Ze University, 135 Yuan-Tung Road, Chungli, 320 Taoyuan, Taiwan, ROC
[b] Energy & Environmental Laboratories, Industrial Technology Research Institute, Taiwan, ROC

## ARTICLE INFO

## ABSTRACT

In this work, a micro-temperature sensor on a 40 μm flexible stainless-steel substrate was fabricated using micro-electro-mechanical systems (MEMS). Embedding a micro-temperature sensor in a proton exchange membrane fuel cell (PEMFC) to monitor temperature will not damage the sensor during the experimental process. This investigation is the first to develop a micro-temperature sensor that can be placed anywhere between the membrane electrode assembly (MEA) and the flow-channel plate inside a PEMFC. The simulated temperature is consistent with the experimentally determined temperature. The performance curve is also consistent with experimental results, revealing the accuracy of the simulation and the effectiveness of monitoring temperature inside a PEMFC.

## 1. Introduction

The environmental consequences of burning fossil fuels in vehicles and the production of electricity have become a major environmental issue that has greatly affected the development of fuel cells [1]. Strict environmental protection laws and the Kyoto Protocol have been established. Fossil fuels are renewable sources of energy and their reserves are being greatly depleted. Therefore, conventional internal-combustion engines that burn fossil fuels should be replaced by cleaner engines. Fuel cells are electrochemical energy-conversion devices that efficiently convert chemical energy that is stored in reactants into electrical energy. These fuel cells produce potentially useful heat and water as the only major byproducts.

Temperature is an important fuel cell parameter, as it significantly affects the performance of proton exchange membrane fuel cells (PEMFCs), especially charge transfer resistance [2], as well as catalytic activity, dehydration of the solid polymer membrane, mass transfer, and heat management [3].

Many methods can be used to measure temperature. They include the use of thermal sensors and the principles of the lifetime-decay method of phosphor thermometry [4]. Fiber Bragg grating sensors have been installed between flow channels in a cathode collector plate of a single cell, distributed uniformly from the inlet to the outlet, to measure temperature [5]. Thin-film thermocouples (TFTCs) have been fabricated on Kapton (polyimide) substrate to measure the internal temperature of a polybenzimidazole (PBI)-based high-temperature PEMFC [6].

In authors' other research, micro-sensors were fabricated on a stainless-steel substrate. However, these micro-sensors are suitable for only a particular type of fuel cell. The fabricated micro-sensors in this study can be used in all types of fuel cell [7]. They are user-friendly and have a wide range of applications. In this investigation, micro-electro-mechanical systems (MEMS)-based fabrication technology was used to fabricate flexible micro-temperature sensors on a stainless-steel foil substrate (SS-304 with a thickness of 40 μm) to monitor temperature *in situ*. The micro-sensors that were fabricated using this approach have the following advantages characteristics: (1) they are small; (2) they are highly sensitive; (3) they are flexible and strong; (4) they can be mass-produced; (5) they can be placed anywhere to make measurements; and (6) and they can be used to make measurements *in situ*.

This study presents the first micro-temperature sensor that can be placed anywhere between the membrane electrode assembly (MEA) and the flow-channel plate inside a PEMFC. Experimental trials without simulation are problematic, and simulation without experimentation is insufficient. Therefore, this investigation includes both simulation and experimentation.

---
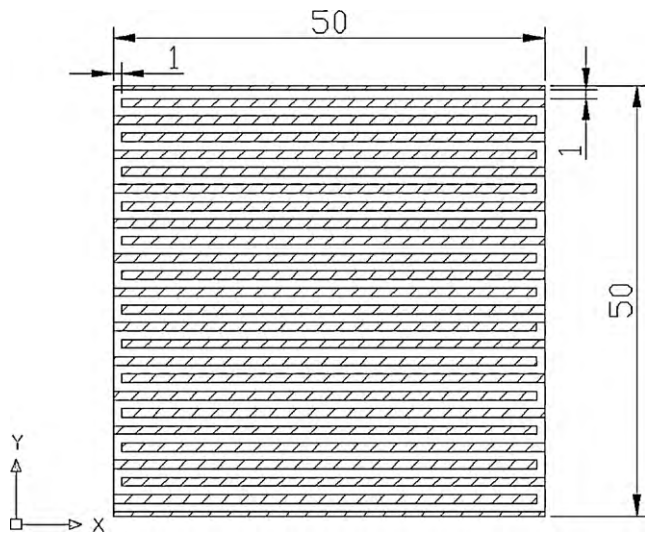
**Fig. 1.** Model geometry and detailed dimensions (shadow region: rib; blank region: channel; unit of length: mm).

**Table 1**
Simulation conditions.

| | |
|---|---|
| Effective diffusivity | Bruggeman, $\tau = 11$ for membrane<br>Bruggeman, $\tau = 1.5$ for GDL and catalyst layer |
| Membrane permeability | $1.8 \times 10^{-18}$ m$^2$ |
| Catalyst layer permeability | $1.76 \times 10^{-11}$ m$^2$ |
| Membrane porosity | 0.28 |
| Catalyst layer porosity | 0.4 |
| Transfer coefficient at anode | 0.5, 0.5 |
| Concentration dependence at anode | 0.5 (H$_2$) |
| Reference current density at anode | $1.0 \times 10^9$ (A m$^{-3}$) |
| Transfer coefficients at cathode | 1.5, 1.5 |
| Concentration dependence at cathode | 1.0 (O$_2$) |
| Reference current density at cathode | $1.5 \times 10^3$ (A m$^{-3}$) |
| GDL and catalyst layer conductivity | 100 $\Omega^{-1}$ m$^{-1}$ |

## 2. Methodology

### 2.1. Micro-temperature sensor

stainless-steel foil with a thickness of 40 μm is used as a flexible substrate. The micro-temperature sensor, fabricated on stainless-steel foil, can be used in a PEMFC to monitor temperature.

A typical temperature sensor has the following four parts; a gold resistance temperature detector (RTD), a thermally sensitive resistor (thermistor), a thermocouple and a mercury-in-glass thermometer. Contact sensors are thermocouples and RTDs; the resistance of these components varies with temperature. Such RTDs comprise resistance wire RTDs and thermistors (thermally sensitive resistors) [8].

Conventional thermocouples are usually used to measure temperature inside fuel cells. Since conventional thermocouples are large and leak fuel, an optimal measurement position cannot be identified. The advantages of an array of RTD micro-sensors are their small volume, high accuracy, short response time, simplicity of fabrication, ease of mass production, and ability to measure temperature more effectively than traditional thermocouples.

The sensing materials most commonly used in temperature sensors are Pt and Au; although Pt is more expensive, Au has better conductivity and flexibility [9,10].

The resistance of a general metal is expressed as

$$R = \rho \frac{L}{A} \tag{1}$$

where $R$ is resistance ($\Omega$); $\rho$ is resistivity ($\Omega$m); $L$ is wire length (m), and $A$ is cross-sectional area (m$^2$). Fig. 1 presents the structure of the micro-temperature sensor. The range of linear variation of resistance of an RTD with temperature, the relationship between measured resistance and change in temperature is given by

$$R_t = R_i(1 + \alpha_T \Delta T), \tag{2}$$

$$\Delta T = t - t_i, \tag{3}$$

where $R_t$ and $R_i$ are the resistance of an RTD at $t$ ($^\circ$C) and $i$ ($^\circ$C), respectively; $\alpha_T$ is the positive temperature coefficient of an RTD; $\Delta T$ is the deviation in temperature from the reference temperature; and $t$ and $t_i$ are temperatures of an RTD at $t$ ($^\circ$C) and $i$ ($^\circ$C),

respectively. Therefore, Eq. (2) can be rewritten as

$$\alpha_T = \frac{R_t - R_i}{R_i(\Delta T)} \tag{4}$$

where $\alpha_T$ is the temperature coefficient of resistance (TCR) of a sensor [11].

### 2.2. Numerical simulations

In order to re-produce the real temperature distribution inside the fuel cell theoretically and compare to the experimental data, the simulation target is to fit the experimental performance curve without any micro-sensors. The dimensions of the simulation model are based on the real fuel cell geometry, as shown in Fig. 1. The computer simulations which we carried out are based on the computational fluid dynamic technique with appropriate electrochemical kinetics. Detail governing equations are listed as follows [12,13].
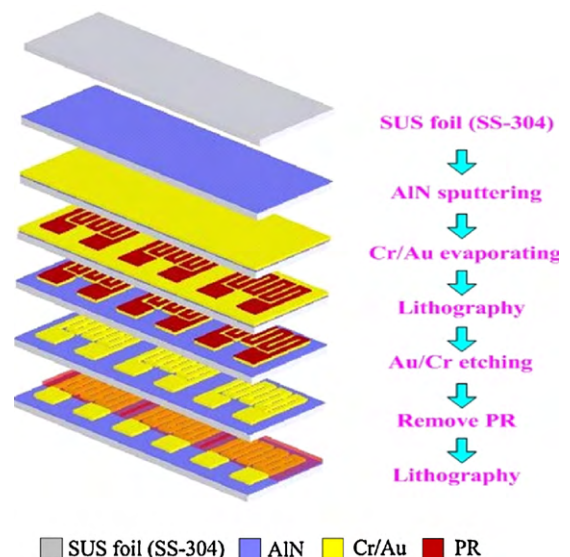


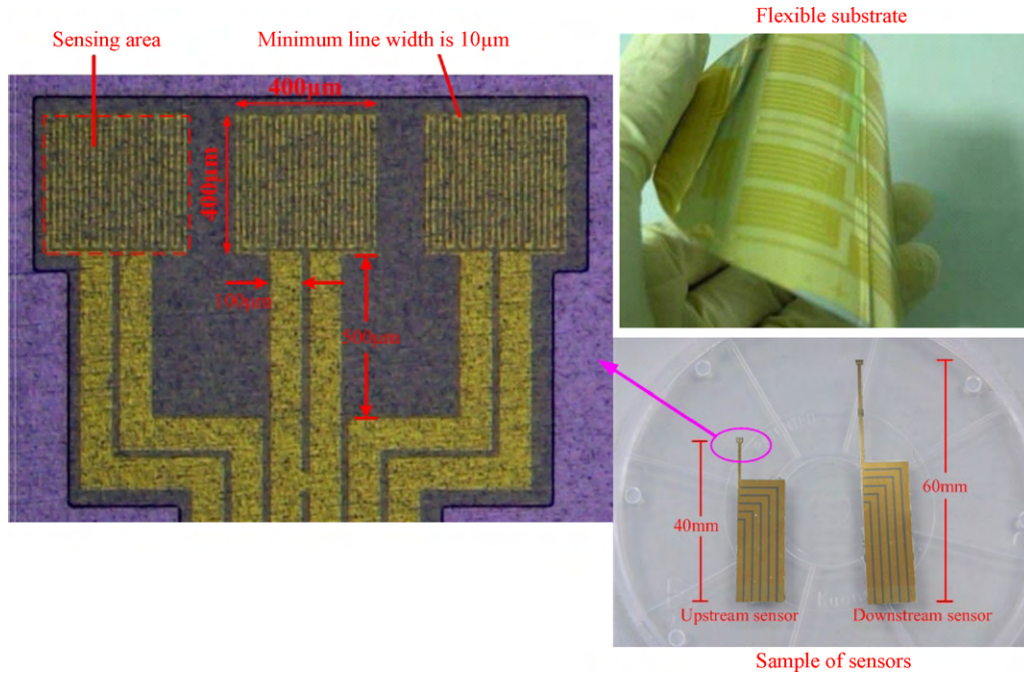**Fig. 2.** Fabrication of flexible micro-temperature sensor.
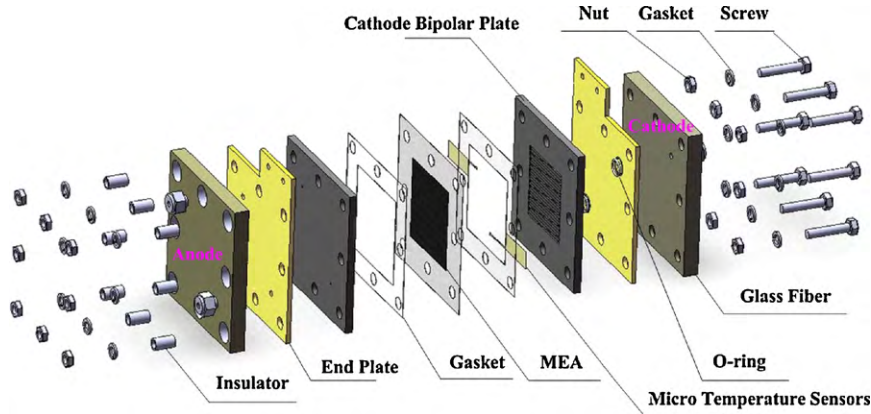
**Fig. 3.** Flexible micro-temperature sensor.



**Fig. 4.** Cell explosion.

### 2.2.1. Channel region

Mass conservation:

$$\nabla \cdot (\rho \vec{U}) = 0, \tag{5}$$

Momentum conservation:

$$\nabla \cdot (\rho \vec{U} u) = -\frac{\partial p}{\partial x} + \nabla \cdot (\mu \nabla u),$$
$$\nabla \cdot (\rho \vec{U} v) = -\frac{\partial p}{\partial y} + \nabla \cdot (\mu \nabla v), \tag{6}$$
$$\nabla \cdot (\rho \vec{U} w) = -\frac{\partial p}{\partial z} + \nabla \cdot (\mu \nabla w)$$

Species conservation:

$$\nabla \cdot (\rho U Y_i) = \nabla \cdot J_i, \tag{7}$$

where $\rho$ indicates density, $U$ indicates velocity vector, u, v and w indicates $x, y$ and $z$ components of the velocity vector, respectively, $p$ indicates pressure and $\mu$ indicates viscosity.

### 2.2.2. Porous region

Mass conservation:

$$\nabla \cdot (\varepsilon \rho U) = 0 \tag{8}$$

Momentum conservation:

$$\nabla \cdot (\varepsilon \rho U U) = -\varepsilon \nabla p + \nabla \cdot (\varepsilon t) + \frac{\varepsilon^2 \mu U}{\kappa}, \tag{9}$$

where $\varepsilon$ indicates porosity, $\kappa$ indicates permeability and $t$ indicates stress tensor.
Species conservation:

$$\nabla \cdot (\varepsilon \rho U Y_i) = \nabla \cdot J_i + \dot{\omega}_i, \tag{10}$$

where $J$ indicates diffusive flux and $\dot{\omega}_i$ indicates source term due to electrochemical reactions. The diffusive flux can be expressed as

$$J_i = \rho D_i \nabla Y_i + \frac{\rho Y_i}{M} D_i \nabla M - \rho Y_i \sum_j D_j \nabla Y_j - \rho Y_i \frac{\nabla M}{M} \sum_j D_j Y_i, \tag{11}$$
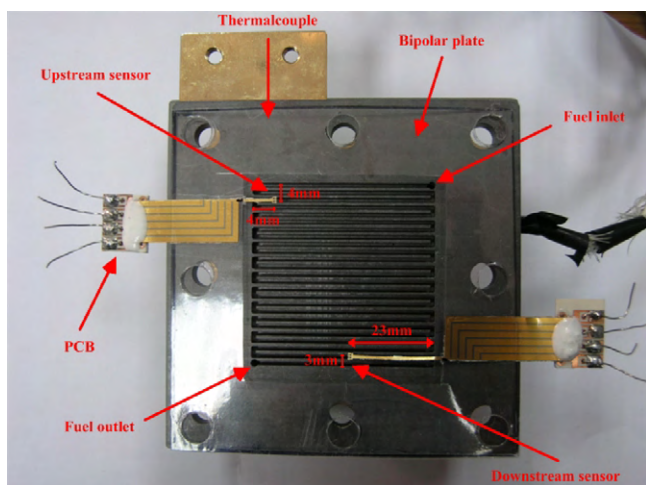
**Fig. 5.** Location of flexible micro-temperature sensor.

where $M$ indicates mixed molecular weight and $Y$ indicates mass fraction.

Energy conservation:

$$\nabla \cdot (\varepsilon \rho U h) = \nabla \cdot q + \varepsilon \tau \cdot \nabla U - j_T \left(\frac{S}{V}\right)_{eff} \eta + \frac{|i \cdot i|}{\sigma}, \qquad (12)$$

The transfer current can be expressed as

$$j_{T,j} = \frac{j_{0,j}}{\prod_{k=1}^{N} [\Lambda_{k,ref}]^{\alpha_{k,j}}} \left[ \exp\left(\frac{\alpha_{a,j}F}{RT}\eta\right) - \exp\left(\frac{\alpha_{c,j}F}{RT}\eta\right) \right]$$
$$\times \prod_{k=1}^{N} [\Lambda_k]^{a_{k,j}}, \qquad (13)$$

where $h$ indicates enthalpy, $q$ indicates conductive heat flux, $J_T$ indicates transfer current, $(S/V)_{eff}$ indicates effective surface to volume ratio, $\eta$ indicates overpotential, $\sigma$ indicates electrical conductivity, $j_0$ indicates exchange current density, $[\Lambda]$ indicates molar concentration, $\alpha$ indicates transfer coefficient, $R$ indicates gas constant and $F$ indicates Faraday constant.

Potential conservation:

$$\nabla \cdot (\sigma_F \nabla \Phi_F) = -\nabla \cdot (\sigma_S \nabla \Phi_S) = j_T \left(\frac{S}{V}\right)_{eff}, \qquad (14)$$

where $\Phi_F$ and $\Phi_s$ indicate ionic and electrical potential, respectively.

The effective transport parameters (diffusivity and conductivity etc) are all estimated by the Bruggeman relation:

$$\psi_{eff} = \psi_{bulk} \varepsilon^{\tau}. \qquad (15)$$

where $\psi$ indicates corresponding transport parameters and $\tau$ indicates tortuosity.
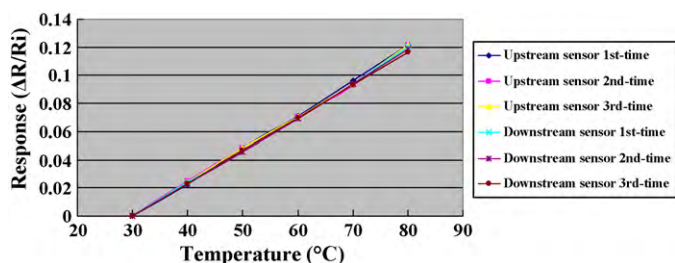
**Table 2**
Operating conditions.

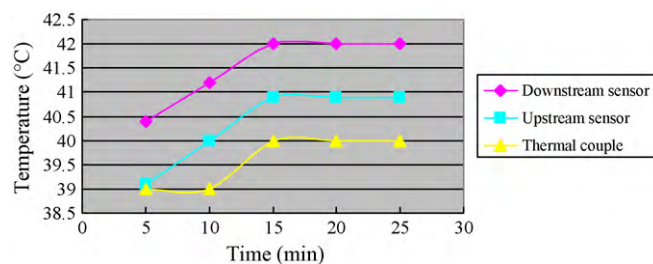| Items | Conditions |
|---|---|
| Cell temperature | 40 °C, 50 °C, 60 °C |
| Relative humidity (%RH) | 100% |
| $H_2$ flow rate (anode) | 380 sccm ($\lambda = 2x$ at $1\,A\,cm^{-2}$) |
| Air flow rate (cathode) | 905 sccm ($\lambda = 2x$ at $1\,A\,cm^{-2}$) |
| Bipolar plate/flow field type | Graphite/single-path serpentine |
| Flow-channel depth | 1 mm |
| Flow-channel width | 1 mm |
| Flow-rib width | 1 mm |
| Reaction area | 25 cm$^2$ |



**Fig. 7.** Temperature distribution curve for constant output current of 2.5 A (cell temperature, 40 °C).

With all the above governing equations, boundary conditions are applied on all boundaries according to the real operation conditions. The flow rate, mass fractions and temperature are applied at the inlet boundaries. All the wall boundaries are set to be corresponding wall conditions (no-slip and insulation etc). Detailed simulation parameters are shown in Table 1.

## 3. Fabrication of micro-temperature sensor

In this work, micro-temperature sensors were fabricated on a stainless-steel foil substrate (SS-304, 40 μm thick), and aluminum nitride (AlN) was applied as an insulation layer because it has excellent insulation properties and thermal conductivity.

Fig. 2 displays the process for fabricating the flexible micro-temperature sensor. First, sulfuric acid and hydrogen peroxide are used to clean the stainless-steel foil; AlN is then sputtered (1 μm) as the bottom insulation layer. An E-beam evaporator is then used to evaporate Cr (400 Å) as an adhesive layer between the AlN and Au. Evaporated Au (2200 Å) is deposited as the sensing layer. The photoresist (PR) is then spin-coated (3 μm) and the outline of the micro-temperature sensor is defined lithographically by wet etching. The PR was again spin-coated (5 μm) as a protection layer. Finally, the stainless-steel foil was etched using aqua regia.



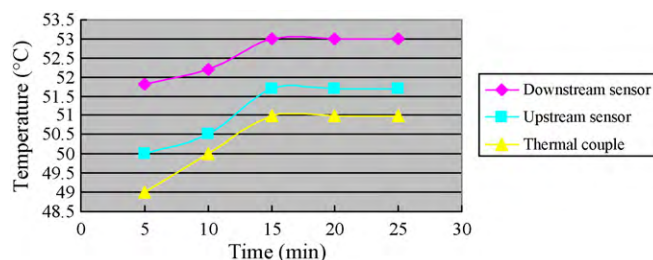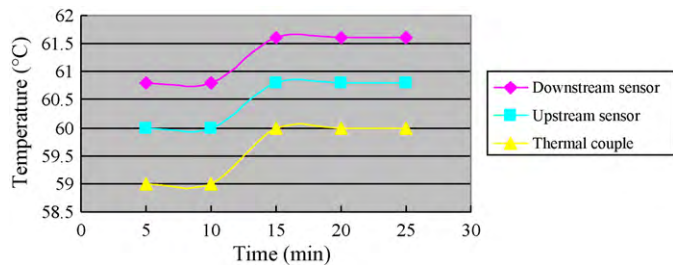**Fig. 6.** Calibration curve of flexible micro-temperature sensor.



**Fig. 8.** Temperature distribution curve for constant output current of 2.5 A (cell temperature, 50 °C).

**Table 3**
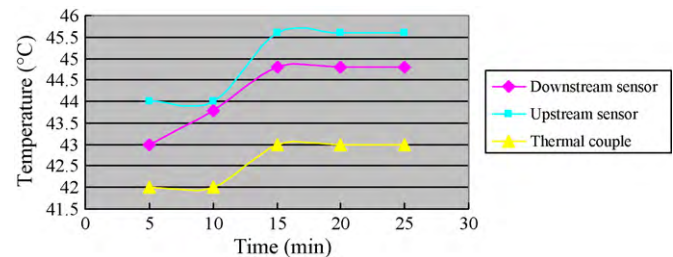Activation procedure of MEA for the PEMFC polarization experiments.

| Protocol step | Time (min) | Voltage (mV) | Current density (mA cm$^{-2}$) | Temperature (°C) | Pressure (kPa) | Stoich. ratio | |
|---|---|---|---|---|---|---|---|
| | | | | | | H$_2$ | Air |
| Initial startup–heat-up and humidification | As needed | 0 | 0 | 65 | 0 | 2.0 (N$_2$) | 2 |
| Pre-conditioning cycling step repeat 12 times | 10 | 200 | Run cycling test at constant flow rate based on 2 stoich. and 1500 mA cm$^{-2}$ | 85 | 170 | Base SCCM flow rate on 2 stoich. and 1200 mA cm$^{-2}$ 2 | 2 |
| | 0.5 | 1000 | | | | Base SCCM flow rate on 2 stoich. and 1500 mA cm$^{-2}$ | |
| Simple pole run 2 times | 20 | | 1200 | 85 | 170 | 2 | 2 |
| | 20 | | 1000 | | | | |
| | 20 | | 800 | | | | |
| | 20 | | 600 | | | | |
| | 20 | | 400 | | | | |
| | 20 | | 200 | | | | |
| | 20 | | 100 | | | | |
| Performance qualification run 2 times | 30 | | 1400 | 65 | 0 | 1.25 | 1.67 |
| | 30 | | 1200 | | | | |
| | 30 | | 1000 | | | | |
| | 30 | | 800 | | | | |
| | 30 | | 600 | | | | |
| | 30 | | 400 | | | | |
| | 30 | | 200 | | | | |
| | 30 | | 100 | | | | |



**Fig. 9.** Temperature distribution curve for constant output current of 2.5 A (cell temperature, 60 °C).



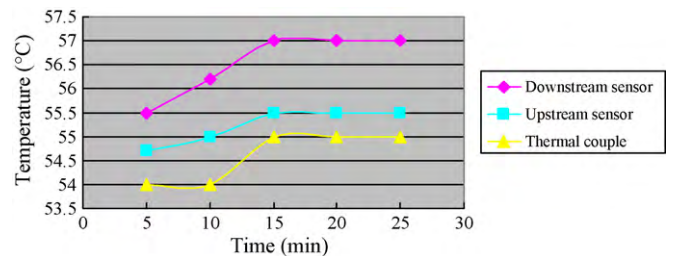**Fig. 11.** Temperature distribution curve for constant output current of 25 A (cell temperature, 50 °C).

## 4. Results and discussion

In this investigation, MEMS technology was used to fabricate a flexible micro-temperature sensor on stainless-steel foil. The fabrication parameters were calibrated experimentally and optimized.

Increasing the insulating area of the flexible micro-temperature sensor worsened PEMFC performance. Therefore, wet etching was used to minimize the insulating area. The authors had previously placed a flexible micro-temperature sensor in a PEMFC and found that the sensor was not damaged during the activation process. The



**Fig. 10.** Temperature distribution curve for constant output current of 25 A (cell temperature, 40 °C).
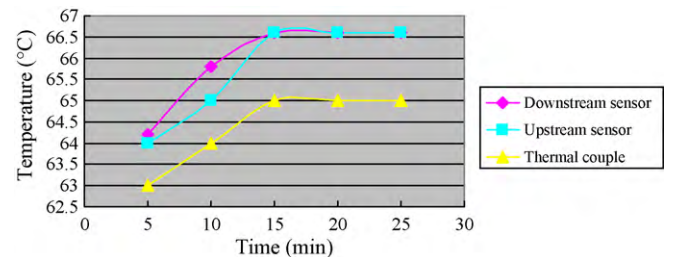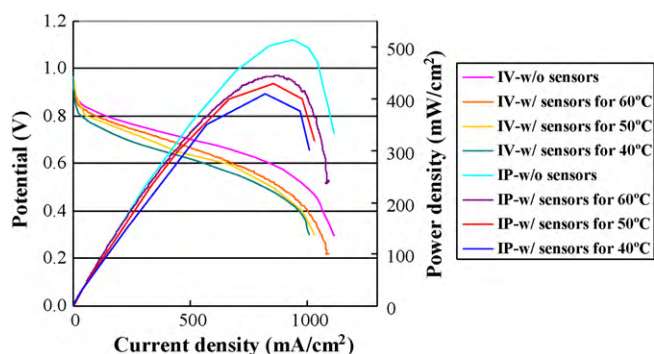


**Fig. 12.** Temperature distribution curve for constant output current of 25 A (cell temperature, 60 °C).

**Fig. 13.** Comparison of cell performance with and without micro-temperature sensors.
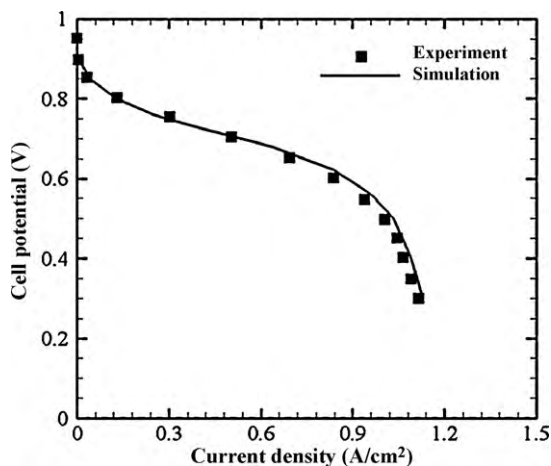


**Fig. 14.** Simulated and experimental performance curves.

assembly pressure reached 15 kg cm$^2$ and data were obtained from within the PEMFC.

Fig. 3 shows a sample flexible micro-temperature sensor. The sensing area of the micro-temperature sensor was 160,000 μm$^2$. The flexible micro-temperature sensor was fabricated using MEMS technology. Such a micro-sensor has the advantages of (1) small size, (2) high sensitivity, (3) high flexibility and strength, (4) mass-producibility, (5) being able to be used in any position and (6) effectiveness in *in situ* measurements.
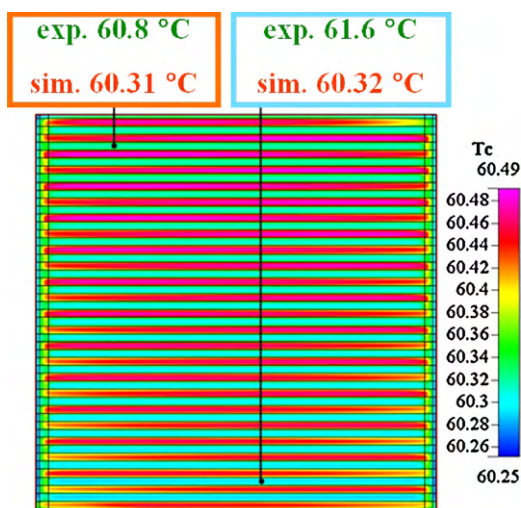


**Fig. 15.** Temperature distribution between flow field plate and GDL with low current density (cell temperature, 60 °C).
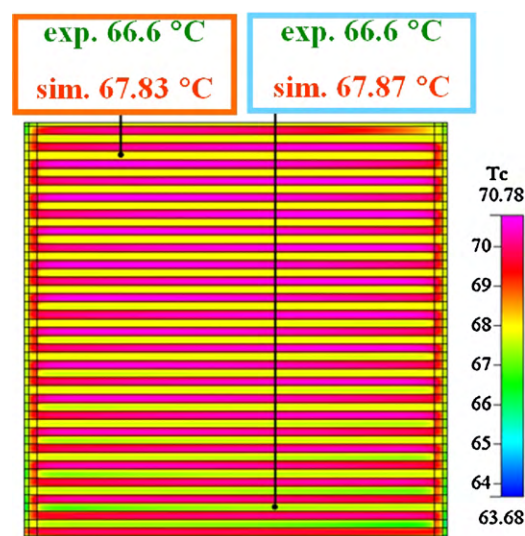


**Fig. 16.** Temperature distribution between flow field plate and GDL with high current density (cell temperature, 60 °C).

Fig. 4 plots the cell explosion. Two embedded flexible micro-temperature sensors can provide data from inside a PEMFC (Fig. 5), allowing the temperature distribution upstream and downstream to be determined precisely.

Fig. 6 plots the calibration curve of the micro-temperature sensor. Each micro-temperature sensor was placed in a programmable temperature chamber, a Hungta HT-8045A. The resistance of the micro-temperature sensor was measured using an LCR meter. The temperature measured by the micro-sensor varied from 30 to 80 °C. The results reveal that the temperature was almost linearly related to resistance. In three tests, the calibration curve was linear. The sensitivity of the micro-temperature sensor was $0.8 \pm 0.005 \, \Omega \, °C^{-1}$, and the accuracy was less than 0.3 °C. The duration of the response was 1.7–2.3 s, measured in the Hungta HT-8045A programmable temperature chamber.

### 4.1. Constant 2.5 A current test

More detail geometry information and operation conditions can be found in Table 2. The activation procedure of MEA for the PEMFC polarization experiments as shown in Table 3. Temperature was operated at 40, 50, and 60 °C with both the anode and the cathode at 100% RH. The gas flow rate of $H_2$ was 380 sccm and that of air was 905 sccm. The output of the cell was a constant current of 2.5 A. Monitoring upstream and downstream temperature took 30 min. Figs. 7 and 8 reveal that that temperature differences between upstream and downstream were 1.1 and 1.3 °C at 40 and 50 °C, respectively. Fig. 9 reveals that that temperature differences between upstream and downstream was 2 °C at 60 °C. The difference between the inner temperature by upstream sensor and outer temperature by thermocouple was around 0.8 °C.

**Table 4**
Comparison of power density with and without micro-temperature sensors.

| | Power density at 0.5 V | Maximum power density |
|---|---|---|
| Without micro-sensors | 505 mW cm$^{-2}$ | 519 mW cm$^{-2}$ |
| With micro-sensors | 443 mW cm$^{-2}$ (degrade 12.3%) | 446 mW cm$^{-2}$ (degrade 14.3%) |

### 4.2. Constant 25 A current test

Figs. 10 and 11 display under the same conditions with a constant output current of 25 A. Those temperatures differences between upstream and downstream were 0.8 and 1.5 °C at 40 and 50 °C, respectively. Fig. 12 reveals that that temperature differences between upstream and downstream was 0 °C at 60 °C. The difference between the inner temperature by upstream sensor and outer temperature by thermocouple was around 1.6 °C.

### 4.3. Polarization curve

Fig. 13 compares experimentally measured cell performance with micro-temperature sensors installed with that without sensors installed. The power density at 0.5 V without a sensor is 505 mW cm$^{-2}$, and that with a sensor is 443 mW cm$^{-2}$. Since the reaction area of a fuel cell with a sensor is less than 1% smaller than that without a sensor, but the performance of the former is 12.3% worse. Table 4 shows the comparison of power density with and without the sensor. In the past, locking pressures of up to 30 kg cm$^2$ have been generated, potentially damaging flexible micro-temperature sensors. The highest locking pressure in this study is only 15 kg cm$^2$. A lack of locking pressure leads to leakage of the fuel cell, and, thereby, worsened performance. Accordingly, the optimized integrated design of fuel cells with flexible micro-temperature sensors should be pursued for *in situ* monitoring and diagnosis.

### 4.4. Comparison of numerical simulations

The experimental data indicate that the discrepancy between results with and without micro-sensors is within the range 5–8% at all operating voltages. Fig. 14 compares the simulation results and the experimental measurements. It reveals high consistency between simulation and experiment. The simulation results must be adjusted to fit the experimental data because the transport phenomena substantially with the fuel cell performance. The simulation parameters exchange current density and tortuosity was tuned to validate the experiments. Tuning these two parameters is reasonable since their exact values are hard to measure. Figs. 15 and 16 demonstrate the temperature distribution between the flow field plate and the gas diffusion layer (GDL) at low and high current density, respectively. At low current density, the difference between the simulated and experimental inlet temperatures are 0.49 °C; the difference at the outlet is 1.28 °C. At high current density, the difference between the simulated and experimental inlet temperatures is 1.23 °C; the difference at the outlet is 1.27 °C. The experimental and simulated inlet and outlet temperatures are fairly close to each other at both high and low current densities. These results further prove that the measurement of temperature by the micro-sensor is sufficiently accurate from the viewpoint of theoretical simulations. The other advantage of the numerical simulation is that it reveals the preferred locations of the micro-sensors. For example, the location of highest temperature gradient or other specific locations, may be of particular interest. These locations are hard to be determined without numerical simulation. Complementary experimental measurements and numerical simulations can increase the effectiveness of *in situ* temperature monitoring inside a fuel cell.

## 5. Conclusion

The temperature field inside a PEMFC was determined from data obtained in the first 15 min of a test using micro-temperature sensors, and indicated that temperature inside a PEMFC was not as stable as when thermocouples were used, perhaps because of instability of the inlet fuel or the operating conditions. Experimentally, the temperature inside the PEMFC increased slowly with the cell current. The greatest difference between the internal and external cell temperature was 2.6 °C. The difference between the performance curves (Fig. 13) obtained with and without the flexible micro-temperature sensors were was caused by the insulated area occupied by the flexible micro-temperature, resisted the transfer of protons to the cathode and reduced the reaction area of PEMFC.

## References

[1] J. Kim, N. Cunningham, J. Power Sources 195 (2010) 2291.
[2] J.L. Jespersena, E. Schaltzb, S.K. Karb, J. Power Sources 191 (2009) 289.
[3] J. Lebæk, S.T. Ali, P. Møller, C. Mathiasen, L.P. Nielsen, S.K. Kær, Int. J. Hydrogen Energy (in press), doi:10.1016/j.ijhydene.2009.10.002.
[4] K. Inman, X. Wang, B. Sangeorzan, J. Power Sources 195 (2010) 4753.
[5] N.A. David, P.M. Wild, J. Hu, N. Djilali, J. Power Sources 192 (2009) 376.
[6] S.T. Ali, J. Lebæk, L.P. Nielsen, C. Mathiasen, P. Møller, S.K. Kær, J. Power Sources 195 (2010) 4835.
[7] C.Y. Lee, W.Y. Fan, W.J. Hsieh, Sensors 10 (2010) 6395.
[8] J.J. Park, M. Taya, J. Electron. Packaging 127 (2005) 286.
[9] C.Y. Shih, Y. Chen, J. Xie, Q. He, Y.C. Tai, J. Chromatogr. A 1111 (2006) 272.
[10] K.L. Zhang, S.K. Chou, S.S. Ang, Int. J. Therm. Sci. 46 (2007) 580.
[11] J.S. Wilson, Sensor Technology Handbook, Butterworth-Heinemann, Boston, 2004.
[12] S. Mazumder, J.V. Cole, J. Electrochem. Soc. 150 (2003) A1503.
[13] S. Mazumder, J.V. Cole, J. Electrochem. Soc. 150 (2003) A1510.